Transient Chip-Package Cosimulation of Multiscale Structures Using the Laguerre-FDTD Scheme

Myunghyun Ha, Krishna Srinivasan, and Madhavan Swaminathan

***Abstract*—Transient simulation using Laguerre polynomials is unconditionally stable and is ideally suited for modeling structures containing both small and large feature sizes. The focus of this paper is on the automation of this technique and its application to chip-package cosimulation. Laguerre finite-difference time-domain (FDTD) requires using the right number of basis coefficients to generate accurate time-domain waveforms. A method for generating the optimal number of basis functions is presented in this paper. Equivalent circuit models of the FDTD grid have been developed. In addition, a method for simulation over a long time period is also presented that enables the extraction of the frequency response both at low and high frequencies. A node numbering scheme in the circuit model of the FDTD grid that is suitable for implementation has been discussed. Results from a chip-package example that shows the scalability of this technique to solve multiscale problems have been presented.**

***Index Terms*—Finite-difference time-domain (FDTD), Laguerre, unconditionally stable.**

I. Introduction

TRANSIENT simulation using Laguerre polynomials is unconditionally stable and therefore, has the advantage of not being limited by the time step. Laguerre-FDTD was first proposed in [1] and has shown to be 70–80× faster than the conventional FDTD scheme for multiscale simulation. The unconditionally stable nature of transient simulation using Laguerre polynomials has been exploited to fix the late-time instability problem in the time-domain electric-field integral equations in [2]. Laguerre-FDTD has also been used to obtain wideband frequency response efficiently in [3]. In this paper, the Laguerre-FDTD method has been applied to packaging problems.

A property of the chip-package structure is the multiscale feature. The on-chip structures require a very fine mesh for simulation, and therefore the time step resulting from the well known Courant condition can become prohibitively small. The alternating direction implicit-FDTD (ADI-FDTD) scheme can be used to speed up simulation and has been shown to provide a $10\times$ improvement in the simulation time in [4]. Also, multiresolution time-domain (MRTD) scheme using scaling and wavelet functions has been shown to provide savings of an order of magnitude with respect to execution time [5], and Holland's method proposed in [6] has been used to enhance simulation time by avoiding fine meshing for thin wires, by modeling the thin wires with a cell size smaller than the FDTD cell. Laguerre-FDTD, however, can be significantly faster than FDTD and other time domain methods especially for packaging problems containing multiscale dimensions. By using an implicit solution technique, a decrease in simulation time has been achieved at the expense of increased memory.

Since the introduction of Laguerre FDTD in [1], several modifications have been made to the algorithm. In [7], a method using Laguerre-FDTD for simulating for long time duration has been presented. In [8], an equivalent circuit model of the FDTD grid has been developed, thereby reducing the matrix size that needs to be solved. This method has been applied to both electromagnetic and circuit problems consisting of inductors, resistors, and capacitors in [8]. In this paper, two enhancements to the Laguerre-FDTD method presented in [7]–[10] have been described. Since Laguerre basis functions decay rapidly in time, application of the Laguerre-FDTD method for long time simulation is still a challenge. Also, a method is presented that provides a solution which is far superior to the solution technique in [7], and therefore provides a frame work for simulation over extended time periods. In addition, a method for choosing the optimal number of basis functions using the L^1 norm is presented. Though this is an extension of [11] and [12], mathematical details that support this scheme have been presented in this paper in addition to its application on several packaging examples.

The modified algorithm discussed in this paper has been named SLeEC, which stands for Simulation using LaguerrE Equivalent Circuit. The major contributions of this paper are as follows.

1) Reformulation and application of the Laguerre-FDTD method for long time duration of 1 μs or higher arising in chip-package problems.
2) Choosing the optimal number of basis function in the Laguerre-FDTD method with underlying mathematical justification.

In addition, the minor contribution of the paper includes a node numbering scheme using Laguerre polynomials that leads to the sparsity in the 3-D FDTD grid and application of the SLeEC method to several structures arising in chip-package problems with mutilscale dimensions.

The remaining paper is organized as follows. An overview of the SLeEC methodology is given in Section II. Representation

Manuscript received June 07, 2008; revised November 10, 2008; February 01, 2009. First published July 24, 2009; current version published November 04, 2009. This work was supported by the Mixed Signal Design Tools Consortium (MSDT), Georgia Tech under Project 2126Q0R. This work was recommended for publication by Associate Editor M. Nakhla upon evaluation of the reviewers comments.

The authors are with the Department of Electrical and Computer Engineering, Georgia Institute of Technology, Atlanta, GA 30332 USA.

Color versions of one or more of the figures in this paper are available online at http://ieeexplore.ieee.org.

Digital Object Identifier 10.1109/TADVP.2009.2020518

1521-3323/$26.00 © 2009 IEEE

Authorized licensed use limited to: Georgia Institute of Technology. Downloaded on November 19, 2009 at 13:11 from IEEE Xplore. Restrictions apply.

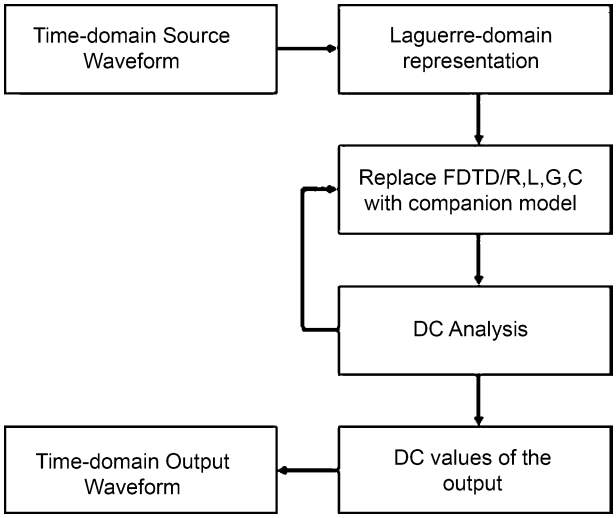

Fig. 1. Flowchart of the SLeEC methodology.

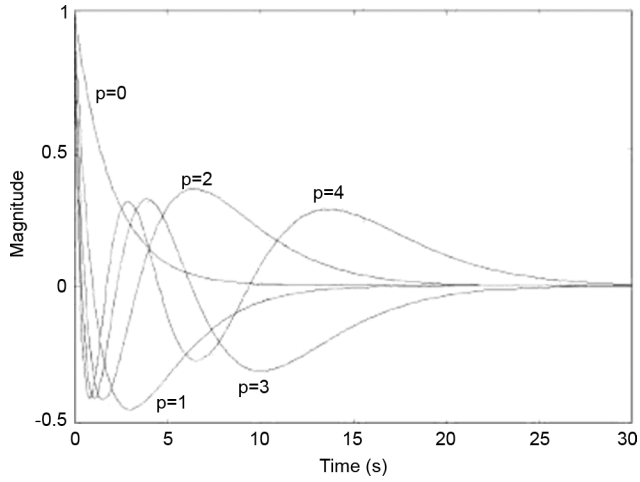

Fig. 2. Laguerre basis functions for order $p = 0 - 4$ [1].

of a time-domain source waveform using Laguerre basis functions is described in Section III. The equivalent circuit model of the FDTD grid is presented in Section IV. In Section V, a new formulation for simulating over long time is described along with an example. In Section VI, a method for choosing the optimal number of basis function is described. In Section VII, a node numbering scheme that enables matrix sparsity is presented followed by several test cases in Section VIII. Conclusions are presented in Section IX.

II. SLeEC Methodology

The transient EM simulation methodology using Laguerre-FDTD is shown in Fig. 1[11].

The first step in the flow chart is to convert the source representations from the time domain into the Laguerre domain. A time-domain source waveform is represented by a set of coefficients in the Laguerre domain. The FDTD grid is next replaced by an equivalent companion model composed of resistors, voltage controlled current sources and independent current sources. The companion model of the 3-D FDTD grid is described in detail in Section IV. A series of dc analyses are done on the circuit model of the FDTD grid, where each of the coefficients that represents the source waveform is used as an independent dc current source. In the circuit model of the FDTD grid, the dc solution of the nodal voltages represent the electric-field Laguerre coefficients and the branch currents represent the magnetic-field Laguerre coefficients. For each of the coefficients that represents the source waveform, a dc analysis is done only once. At the end of the dc analysis, the solution is used to update the companion model before the next dc analysis is done using the next value of the Laguerre-domain coefficient of the source waveform. The final step is to convert the values obtained from the dc solution of the output field of interest into time-domain waveform. In this step, choosing the optimal number of basis coefficients is essential to maximizing accuracy. Analytical formulae have been given in [1] to determine the correct number of basis functions. The analytical formulae however provide a range of values for the number of basis functions that can be used. Test cases that have been simulated in this paper show that this number has to be of a specific value which is determined best through numerical analysis.

III. Laguerre-Domain Representation of Source Waveforms

In the SLeEC method, the time-domain source waveforms have to be converted into equivalent Laguerre-domain representations. A transient source waveform $W(t)$ can be represented as a sum of N Laguerre basis functions $\varphi_p(\bar{t})$, scaled by Laguerre basis coefficients W_p as shown in (1) [1]

$$W(t) = \sum_{p=0}^{p=N-1} W_p \varphi_p(\bar{t}) \tag{1}$$

$$\bar{t} = s \cdot t. \tag{2}$$

In (2), $\bar{t}$ is dimensionless and representing the real time t multiplied by a scaling factor s. This is done to increase the time scale to the order of seconds. The basis functions for orders $p = 0-4$ are plotted in Fig. 2 [1]. The basis functions span a time in the order of seconds as shown by the x-axis in Fig. 2, hence the need for the scale factor arises.

The definition of the basis function is shown

$$\varphi_u(\bar{t}) = e^{-\bar{t}/2} L_u(\bar{t}). \tag{3}$$

Laguerre polynomials are defined recursively as follows:

$$L_0(\bar{t}) = 1 \tag{4}$$

$$L_1(\bar{t}) = 1 - \bar{t} \tag{5}$$

$$pL_p(\bar{t}) = (2p - 1 - \bar{t}) L_{p-1}(\bar{t}) - (p-1) L_{p-2}(\bar{t}), \quad \text{for } p \geq 2. \tag{6}$$

The transient source waveforms are replaced by equivalent dc sources. The values of the dc sources are the set of Laguerre basis coefficients $\{W_p\}$, which represent the transient source waveform in the Laguerre-domain. $\{W_p\}$ is generated from $W(t)$ using

$$W_p = \int_0^\infty W(t) \varphi_p(\bar{t}) d\bar{t}. \tag{7}$$

Authorized licensed use limited to: Georgia Institute of Technology. Downloaded on November 19, 2009 at 13:11 from IEEE Xplore. Restrictions apply.

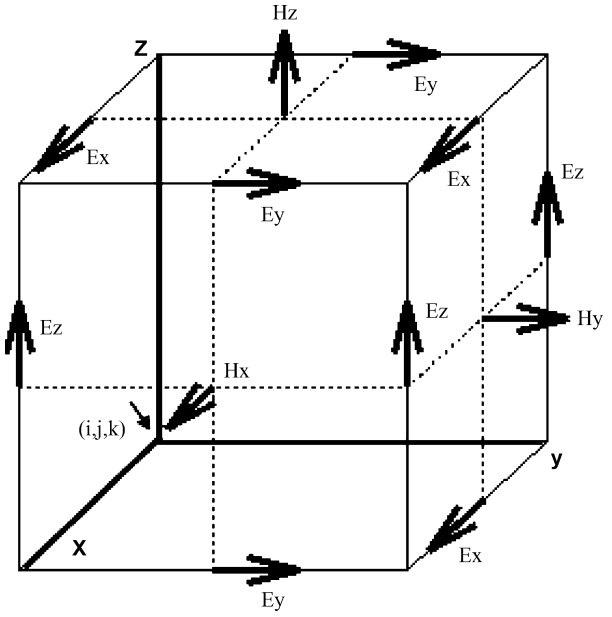

Fig. 3. Standard Yee cell.

Laguerre basis functions satisfy the orthonormal property

$$\int_0^\infty \varphi_u(\bar{t})\varphi_v(\bar{t})d\bar{t} = \delta_{uv}. \tag{8}$$

In (8), δ_{uv} is the Kronecker delta function. Equation (7) can be derived by multiplying both sides of (1) with $\varphi_q(\bar{t})$, integrating the two sides from $[0,\infty]$ and using the orthonormal property given by (8). Laguerre polynomials also satisfy the relationship given in (9), which can be obtained by observing that $\varphi_p(0) = 1$ for all values of p

$$\int_0^\infty \delta(t)\varphi_p(\bar{t})d\bar{t} = s\varphi_p(0) = s. \tag{9}$$

The output of *Laguerre-domain representation* in Fig. 1 is to compute the set of Laguerre basis coefficients $\{W_p\}$ that represents each of the transient source waveforms.

IV. Equivalent Circuit Model Representation of the FDTD Grid

The standard FDTD Yee cell is shown in Fig. 3 [13]. The cross sections of the FDTD cell at the locations marked by the dotted lines in Fig. 3 are shown in Fig. 4. These represent the cross sections as viewed by standing on the $+\infty$ of y, x, and z axis and facing the Yee cell. A circuit model that represents the Laguerre basis coefficients of the fields has been derived in [10], where the nodal voltages represent the basis coefficients of the electric fields and the branch currents represent the magnetic fields.

Consider the following two of six Maxwell's differential equations:

$$\frac{\partial H_z}{\partial t} - H_z^{init}\delta(t) = \frac{1}{\mu}\left(\frac{\partial E_x}{\partial y} - \frac{\partial E_y}{\partial x}\right) \tag{10}$$

$$\frac{\partial E_y}{\partial t} - E_y^{init}\delta(t) = \frac{1}{\epsilon}\left(\frac{\partial H_x}{\partial z} - \frac{\partial H_z}{\partial x} - J_y\right). \tag{11}$$

The initial conditions are explicitly included in the differential equations before converting them to the Laguerre domain, to enable restarting a simulation beyond a certain time duration, as explained in [7]. Using the procedure similar to [7], the time-domain differential (10) and (11) can be converted to the Laguerre domain, given by

$$\begin{aligned} H_z^q|_{i+1/2,j+1/2,k} - 2H_z^{init}|_{i+1/2,j+1/2,k} \\ = -C_x^H|_{i,j,k}\left(E_y^q|_{i+1,j+1/2,k} - E_y^q|_{i,j+1/2,k}\right) \\ +C_y^H|_{i,j,k}\left(E_x^q|_{i+1/2,j+1,k} - E_x^q|_{i+1/2,j,k}\right) \\ -2\sum_{k=0,q>0}^{q-1} H_z^k|_{i+1/2,j+1/2,k} \end{aligned} \tag{12}$$

$$\begin{aligned} E_y^q|_{i,j+1/2,k} - 2E_y^{init}|_{i,j+1/2,k} \\ = -C_x^E|_{i,j,k}\left(H_z^q|_{i+1/2,j+1/2,k} - H_z^q|_{i-1/2,j+1/2,k}\right) \\ +C_z^E|_{i,j,k}\left(H_x^q|_{i,j+1/2,k+1/2} - H_x^q|_{i,j+1/2,k-1/2}\right) \\ -\frac{2}{s\epsilon}J_y^q|_{i,j+1/2,k} - 2\sum_{k=0,q>0}^{q-1} E_y^k|_{i,j+1/2,k}. \end{aligned} \tag{13}$$

Equations (12) and (13) can be represented in a circuit form as given in Fig. 5. Fig. 5 represents the circuit model for the magnetic field $H_z^q|_{i+1/2,j+1/2,k}$ and the electric field $E_y^q|_{i,j+1/2,k}$, at the location marked by the solid edges and their intersection in Fig. 4. Only the partial 3-D model is given in Fig. 5. The complete model can be derived in a similar fashion.

The branch currents represent the qth Laguerre basis coefficient of the magnetic fields and are given by

$$\begin{aligned} H_z^q|_{i+1/2,j+1/2,k} &= I_{i+1/2,j+1/2,k} \\ H_z^q|_{i-1/2,j+1/2,k} &= I_{i-1/2,j+1/2,k} \end{aligned} \tag{14}$$

$$\begin{aligned} H_x^q|_{i,j+1/2,k+1/2} &= I_{i,j+1/2,k+1/2} \\ H_x^q|_{i,j+1/2,k-1/2} &= I_{i,j+1/2,k-1/2}. \end{aligned} \tag{15}$$

The nodal voltages represent the qth basis coefficient of the electric fields

$$E_y^q|_{i,j+1/2,k} = V_{i,j+1/2,k}. \tag{16}$$

The branch current circuitry represents (12) and the circuitry connected to the node with voltage $V_{i,j+1/2,k}$ represents (13). The values of the branch current circuitry are

$$I_{\text{val},1} = 2H_z^{\text{init}}|_{i+1/2,j+1/2,k} - 2\sum_{k=0,q>0}^{q-1} H_z^k|_{i+1/2,j+1/2,k} \tag{17}$$

$$\begin{aligned} I_{\text{val},2} &= C_y^H\left(V_{i+1/2,j+1,k} - V_{i+1/2,j,k}\right) \\ R_1 &= \frac{1}{C_x^H}. \end{aligned} \tag{18}$$

Authorized licensed use limited to: Georgia Institute of Technology. Downloaded on November 19, 2009 at 13:11 from IEEE Xplore. Restrictions apply.

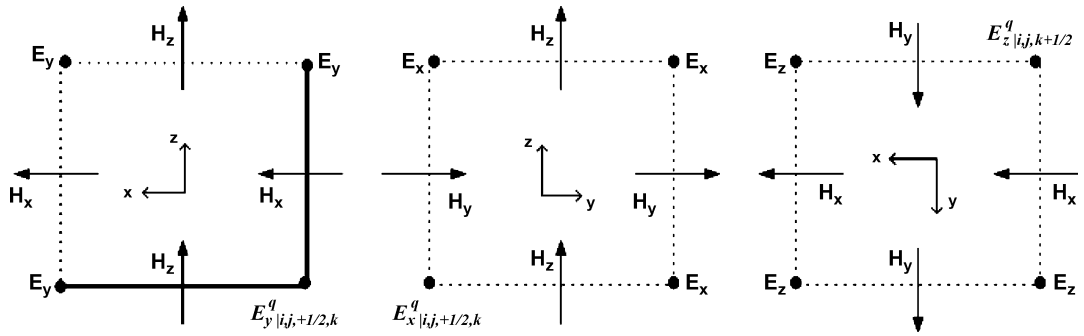

Fig. 4. Sections of the Yee cell marked by the dotted lines in Fig. 3 parallel to the *xz*, *yz*, and *xy* planes, respectively; dots indicate direction of the fields pointing out of the page.

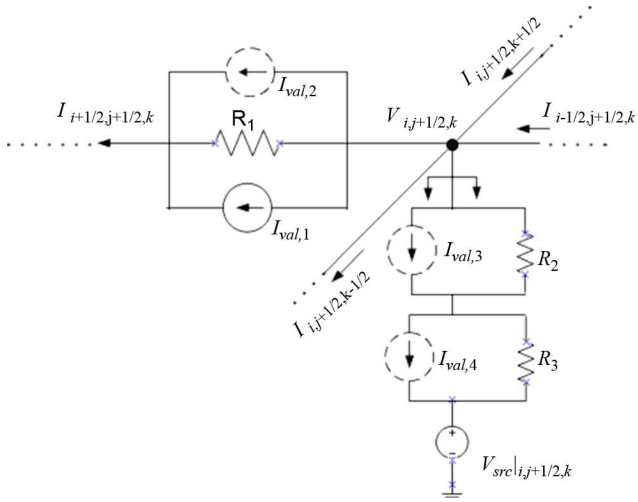

Fig. 5. Companion model of the 3-D FDTD grid in Laguerre domain.

The circuitry connected to the node with voltage $V_{i,j+1/2,k}$ have the values

$$I_{\mathrm{val},3} = I_{i,j+1/2,k+1/2} - I_{i,j+1/2,k-1/2} \tag{19}$$

$$I_{\mathrm{val},4} = I_{i-1/2,j+1/2,k} - I_{i+1/2,j+1/2,k} \tag{20}$$

$$R_2 = C_x^E;\ R_3 = C_z^E \tag{21}$$

$$V_{\mathrm{src}}|_{i,j+1/2,k} = 2E_y^{\mathrm{init}}|_{i,j+1/2,k} - \frac{2}{s\epsilon} J_y^q|_{i,j+1/2,k} - 2\sum_{k=0,q>0}^{q-1} E_y^k|_{i,j+1/2,k}. \tag{22}$$

The circuit given in Fig. 5 can be stamped in a modified nodal analysis (MNA) matrix and solved to find the unknown Laguerre basis coefficients of the electric and magnetic fields. The solution at the end of the qth iteration in the flowchart given in Fig. 1 represents the qth Laguerre basis coefficient of the electric and the magnetic fields. The dc solution at the end of the qth iteration is used to update the companion model before solving for the next set of Laguerre basis coefficients. The number of unknowns that needs to be solved in dc analysis can be reduced by using the Norton equivalent form looking into the circuit marked by the double arrow in Fig. 5. The values of the Norton equivalent circuit are given by

$$I_N = \frac{-I_{val,3}R_2 + V_{\mathrm{src}} - I_{val,4}R_3}{R_2 + R_3}$$
$$R_N = R_2 + R3 \tag{23}$$

I_N has terms involving $I_{\mathrm{val},3}$ and $I_{\mathrm{val},4}$ and is therefore a current controlled current source. In MNA analysis, current controlled current source terms in I_N introduce additional unknowns, besides the unknown nodal voltages [14]. However, I_N can be implemented as voltage controlled current sources and current sources, by stamping the current in a branch directly and the additional unknowns can be eliminated. Voltage controlled current sources do *not* introduce additional unknowns [14]. The unknowns to be solved are *only* the electric field coefficients (nodal voltages) and therefore the matrix dimension to be solved is in its optimal form.

With the values given by (17)–(23), it can be seen from KCL and KVL equations that these satisfy (12)–(13). The partial model in Fig. 5 can be completed in a similar fashion and can satisfy the complete set of 3-D Maxwell's differential equations in the Laguerre domain.

Different types of boundary conditions can be implemented in the companion model. The companion models, besides making the implementation easier, offer a very elegant way to implement the algorithm. The models for the perfect electric conductor (PEC) and the perfect magnetic conductor (PMC) boundary conditions which have been implemented in this paper are presented in the next subsection.

A. PEC Boundary

In the PEC boundary, the tangential electric fields to the boundary are set to zero. As shown in Fig. 6, the PEC boundary is implemented by setting a node to ideal ground. In Fig. 6, the vertical bars represent the positions of the electric fields on the grid and the symbol $\times$ represent the locations of the magnetic fields. The last node, which represents the electric field that is tangential to the boundary, has been set to zero. In SLeEC, the nodal voltages represent the electric-field coefficients. By setting the nodal voltages, which correspond to the tangential electric fields to the boundary to zero, the PEC boundary condition can be implemented.

B. Perfect Magnetic Conductor (PMC) Boundary

In the PMC boundary, the tangential magnetic fields to the boundary are set to zero. As shown in Fig. 7, the PMC boundary is implemented by leaving a branch, whose current corresponds to the magnetic field that is tangential to the boundary, open circuit. In Fig. 7, the vertical bars represent the positions of the electric fields on the grid and the symbols $\times$ represent the locations of the magnetic fields. The current in the last branch,

Authorized licensed use limited to: Georgia Institute of Technology. Downloaded on November 19, 2009 at 13:11 from IEEE Xplore. Restrictions apply.

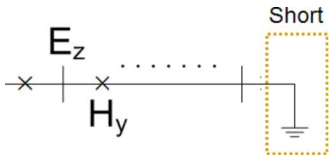

Fig. 6. PEC boundary condition.

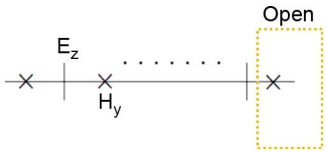

Fig. 7. PMC boundary condition.

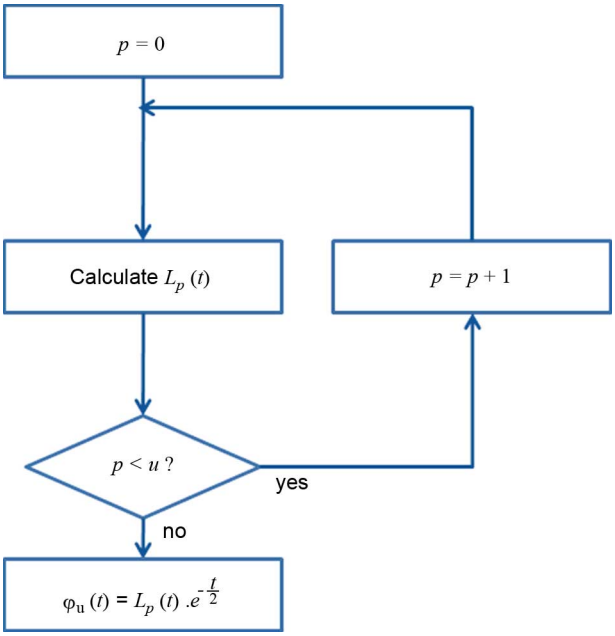

Fig. 8. Algorithm to compute uth Laguerre basis function in [9].

which represents the magnetic-field coefficient that is tangential to the boundary, is set to zero. By leaving the branch as an open circuit, the current through the branch is forced to be zero, thereby implementing the PMC boundary condition.

V. Simulation for Long Time Period

As described earlier, the Laguerre basis functions are as described in (3)–(6). The Laguerre basis functions decay rapidly to zero as in Fig. 2 and hence cannot be used in its present form for simulation over long time period.

Fig. 8 shows the flowchart of the approach used in [9] for computing $\varphi_u(\bar{t})$. By following the recurrence loop in Fig. 8, the Laguerre polynomial $L_p(\bar{t})$ has very large value as order p increases and the magnitude of the basis function's value becomes too large to be represented with limited precision of the computer beyond a large enough order number p and time $\bar{t}$, and therefore overflow occurs. Hence, after some time and order, the basis function no longer has meaningful value as shown in Fig. 10 where the waveform abruptly terminates around $\bar{t} = 1440$. As a solution, [9] divides the total simulation-time into a

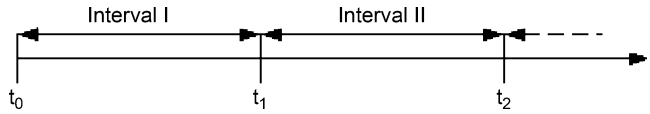

Fig. 9. Total simulation-time is divided into different time-intervals in [9].

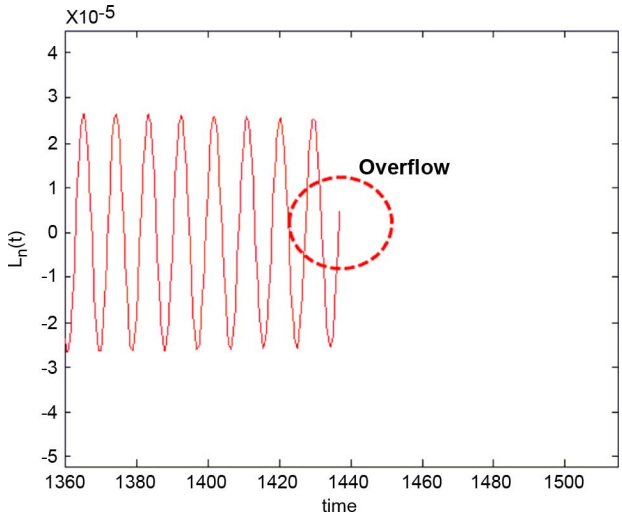

Fig. 10. Calculated 1000th Laguerre basis function by the method in [9] for a multiscale example.

number of short time-intervals and the initial condition of each interval is set to the final condition of the previous interval, as shown in Fig. 9. However, as the number of intervals increases, error accumulates and significant error can occur in later intervals.

The limitations in [9] can be overcome by introducing a balancing process in the recurrence loop, as shown in Fig. 11 [12]. For the balancing process, $\varphi_u(\bar{t})$ is represented as follows:

$$\varphi_p(\bar{t}) = B^m_{p,k}(\bar{t}) \cdot E^m_k \tag{24}$$

where

$$B^m_{p,k}(\bar{t}) = L_p(\bar{t}) \cdot e^{-k/m\bar{t}/2} \tag{25}$$

$$E^m_k(\bar{t}) = e^{-(1-k/m)\cdot\bar{t}/2}. \tag{26}$$

$B^m_{p,k}(\bar{t})$ and $E^m_k(\bar{t})$ in (25) and (26) are called as balanced Laguerre polynomial and balanced exponential function, respectively. $B^m_{p,k}(\bar{t})$ can be calculated by using the recursion in (4)–(6) and (26). New parameters and variables such as θ, m, and k are introduced related to the balancing process. θ is a threshold value that limits the magnitude of the balanced Laguerre polynomial in the recurrence loop. Parameters m and k represent the strength of the balancing process and degree of balancing, respectively. The relation between the balanced Laguerre polynomials before and after incrementing the degree of balancing is

$$B^m_{p,k}(\bar{t}) = B^m_{p,k-1}(\bar{t}) \cdot e^{-1/m\bar{t}/2} \tag{27}$$

where m is selected to ensure $e^{-1/m\bar{t}/2}$ is large enough to avoid overflow problem. For large $\bar{t}$, $e^{-1/m\bar{t}/2}$ can be too small to be represented as a nonzero value in the computer. This should be avoided because $B^m_{p,k}(\bar{t})$ goes to 0 by incrementing the degree of balancing k. Therefore, m needs to be sufficiently large to

Authorized licensed use limited to: Georgia Institute of Technology. Downloaded on November 19, 2009 at 13:11 from IEEE Xplore. Restrictions apply.

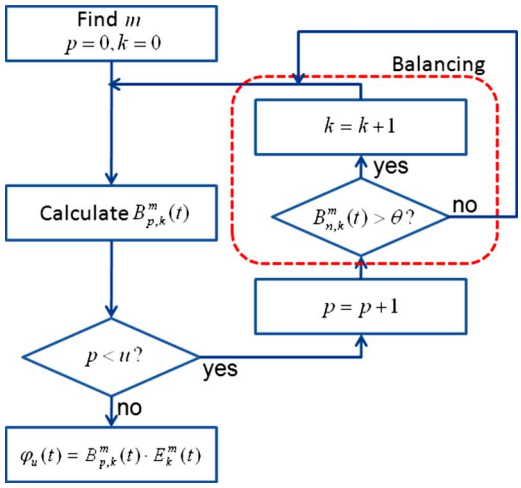

Fig. 11. Proposed algorithm to compute uth Laguerre basis function.

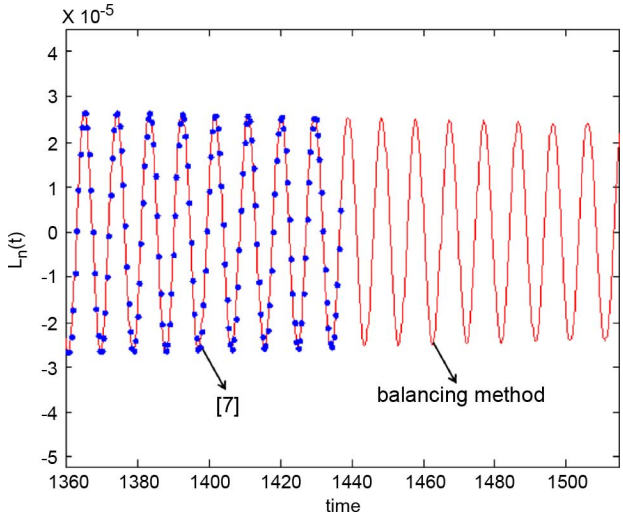

Fig. 12. Calculated 1000th Laguerre basis function by the balancing method for a multiscale example (Dots indicate calculated basis function using [9] for comparison).

ensure $e^{-1/m\bar{t}/2}$ can be represented using finite precision in the computer.

A rule of thumb for representing m in terms of threshold value θ is as follows:

$$m \approx \frac{\bar{t}}{2\ln\theta} \tag{28}$$

resulting in

$$\theta \approx e^{1/m\cdot\bar{t}/2}. \tag{29}$$

If (29) is satisfied, using (28), the magnitude of the balanced Laguerre polynomial goes to 1 as the degree of balancing increases. The balancing process is used for preventing the magnitude of balanced Laguerre polynomial from becoming too large. If the magnitude of the balanced Laguerre polynomial gets larger than the threshold value θ, the balancing process is performed by increasing the degree of balancing k. Since m and $\bar{t}$ have positive values, the magnitude of the balanced Laguerre polynomial reduces as the degree of balancing k increases, as per (25). Therefore, the overflow problem can be avoided since the balanced Laguerre polynomial always remains less than θ in the recurrence loop.

After the computation of $B^m_{p,k}(\bar{t})$, the Laguerre basis function can be calculated using (24). Hence, this formulation enables the application of the Laguerre-FDTD method for computing the response over long time duration.

The computation of the 1000th Laguerre basis function $\varphi_u(\bar{t})$ using the proposed method and the earlier method used in [9] is shown in Fig. 12. The method in [9] cannot calculate the basis function $\varphi_u(\bar{t})$ when $\bar{t}$ is larger than 1440, which is equivalent to 20 ns when the time-scale factor is 7×10^8 , while the proposed method successfully obtains the value of Laguerre basis function at time $\bar{t}$ greater than 1440, as shown in Fig. 12.

VI. Choosing the Optimal Number of Basis Functions

The final step in the SLeEC methodology is to generate the time-domain waveform using the Laguerre basis coefficients of the output of interest. Here, the number of basis functions used in generating the time-domain waveform is very important to obtain accurate results because of the time-domain waveform's sensitivity to the number of basis functions. The methodology used for choosing the optimal number of basis coefficients is explained in detail in the following subsections.

A. Methodology

1) Energy Analysis (Step 1): Laguerre basis functions decay to 0 as time increases, as shown in Fig. 2 and it decays slower as the order of Laguerre basis function increases. Thus, for the later part of a time-domain waveform, which is computed as the sum of weighted Lagurerre basis functions, the number of basis function needs to be sufficiently large. The minimum number of basis functions q_{knee} to represent a time-domain waveform can be found by analyzing the time-domain waveform's energy content as a function of the number of basis functions.

2) Finding the Optimal Number of Basis Functions (Step 2): Given the minimum number of basis functions from Step 1, the correct number of basis functions can be chosen by doing an error analysis. Since the Laguerre basis functions have maximum magnitude at time $t = 0$, minimizing the error at time $t = 0$ is sufficient to determine the exact number of basis coefficients. The optimal number of basis functions q_{opt} is chosen between $\{q_{\text{knee}}, \ldots, q_{\max}\}$ that has the smallest error at time $t = 0$.

By using a source waveform with initial value zero, the field values at all locations also have the value zero at time $t = 0$. By starting the simulation in a known state, the initial value is therefore known. The source waveform used in this paper is a Gaussian pulse shifted in time to ensure zero value at time $t = 0$.

In the next two subsections, the following are discussed.

1) Calculating q_{nee} using the L^1 norm instead of the square of the L^2 norm which provides the minimum number of basis functions required.
2) Minimizing the error at time $t = 0$ to choose the optimal number of basis functions between q_{knee} and $q_{\max}$.

Authorized licensed use limited to: Georgia Institute of Technology. Downloaded on November 19, 2009 at 13:11 from IEEE Xplore. Restrictions apply.

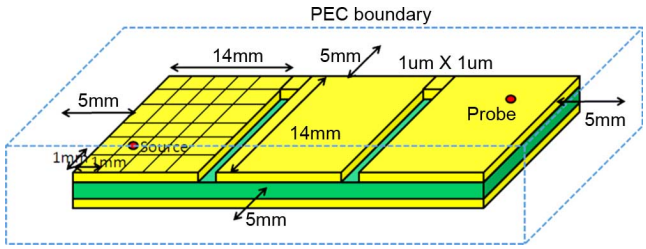

Fig. 13. Planar structure with multiscale features.

B. L^1 Norm Versus L^2 Norm for Calculating q_{knee}

As discussed earlier, the energy contained in the time-domain waveform as a function of the number of basis coefficients needs to be calculated in order to choose the correct number of basis coefficients. The energy can be defined as a summation of the square of the L^2 norm as [11]. An alternate scheme used in this paper for calculating the energy content is defining the energy content as a summation of the L^1 norm.

Consider $E_1(q)$ and $E_2(q)$, which represent the calculated energy content of the time-domain waveform generated using basis coefficients $\{E_0, E_1, \ldots, E_q\}$ with first q basis functions using the L^1 norm and square of the L^2 norm, respectively

$$E_1(q) = \sum_{i=0}^{i=N-1} |W_q[i]| \tag{30}$$

$$E_2(q) = \sum_{i=0}^{i=N-1} |W_q[i]|^2 \tag{31}$$

where W_q is the time-domain waveform obtained using $q+1$ basis coefficients, and N is the number of discrete time points making up the time-domain waveform. In this section, we show that the L^1 norm is better than the L^2 norm for calculating q_{knee}.

The energy's sensitivity to the ith discrete time-domain waveform value can be calculated as

$$S_1(q,i) = \left| \frac{\partial \sum_{i=0}^{i=N-1} |W_q[i]|}{\partial W_q[i]} \right| = 1 \tag{32}$$

$$S_2(q,i) = \left| \frac{\partial \sum_{i=0}^{i=N-1} |W_q[i]|^2}{\partial W_q[i]} \right| = 2|W_q[i]|. \tag{33}$$

Since sensitivity of the energy content using L^2 norm $S_2(q,i)$ is proportional to the magnitude of $W_q[i]$, it is insensitive to small $|W_q[i]|$ s and is dominated by large $|W_q[i]|$ s. Hence, waveforms with large variation in the magnitude can lead to erroneous results at late time when magnitudes become small. On the other hand, the energy content using L^1 norm is equally sensitive to every $W_q[i]$ irrespective of their magnitude. This implies that using L^1 norm will minimize the error at every discrete time of the waveform, as compared to the square of the L^2 norm.

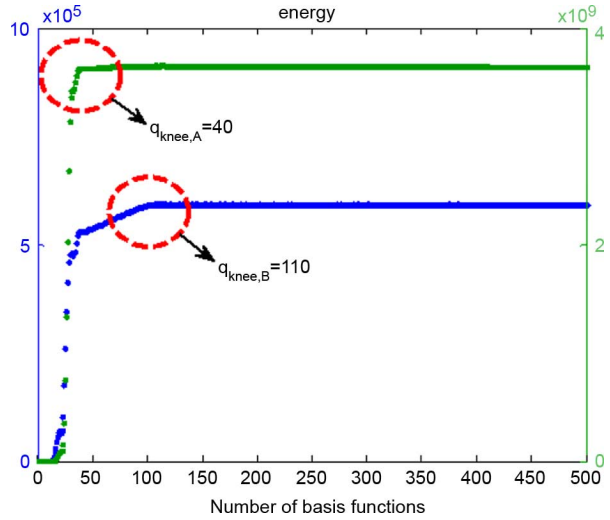

Fig. 14. Energy as a function of the number of basis coefficients using scheme A (the square of L^2 norm) and scheme B (L^1 norm).

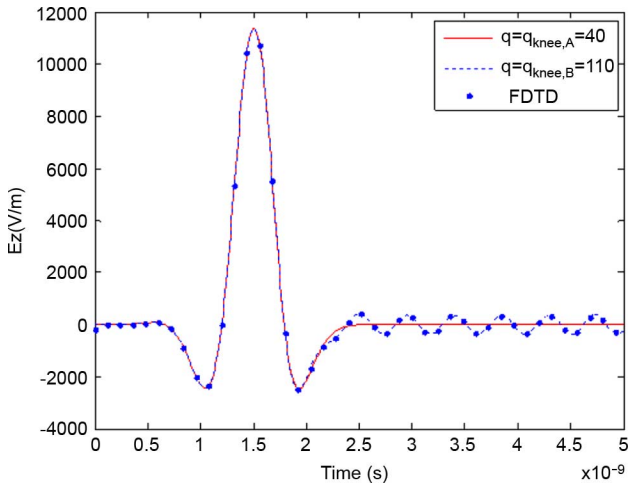

Fig. 15. Time-domain E_z field from q_{knee} basis functions using scheme A and B.

An example shown in Fig. 13 is used to illustrate the advantage of using the L^1 norm instead of the square of the L^2 norm for calculating the minimum number of basis functions.

As shown in Fig. 13, three electromagnetic band gap (EBG) patches with dimension of 14 mm $\times$ 14 mm are connected through 1 μm $\times$ 1 μm bridges. The example has been terminated using a PEC boundary. The number of FDTD cells used in the simulation is $(nx, ny, nz) = (25, 54, 10)$. Modulated Gaussian waveform was used as the source waveform and is located at cell $(19, 8, 0)$, marked *source* in Fig. 13. The electric field E_z is probed at cell $(19, 47, 0)$.

The scheme for choosing the basis coefficients using the energy definition in (30) will be referred to as scheme B while the scheme using L^2 norm is referred to as scheme A. Scheme A and B differ only in the equations used to calculate q_{knee}. Choosing the optimal value for q among the set $\{q_{\text{knee}}, \ldots, q_{\max}\}$ by minimizing the error at time $t = 0$, remains the same for both schemes, as explained in the next subsection.

Authorized licensed use limited to: Georgia Institute of Technology. Downloaded on November 19, 2009 at 13:11 from IEEE Xplore. Restrictions apply.

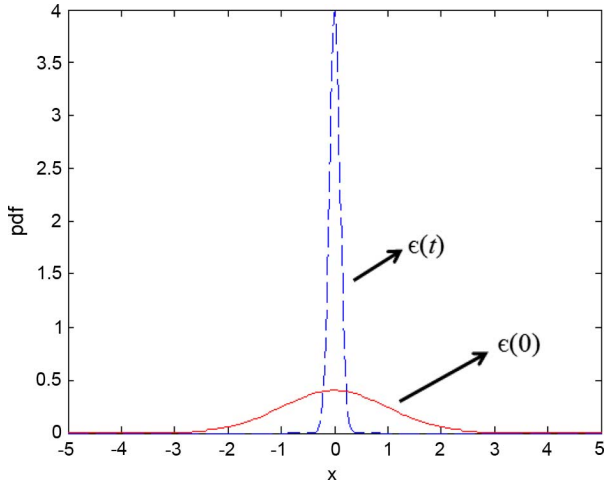

Fig. 16. Probability density functions of normal distribution with large and small variances.

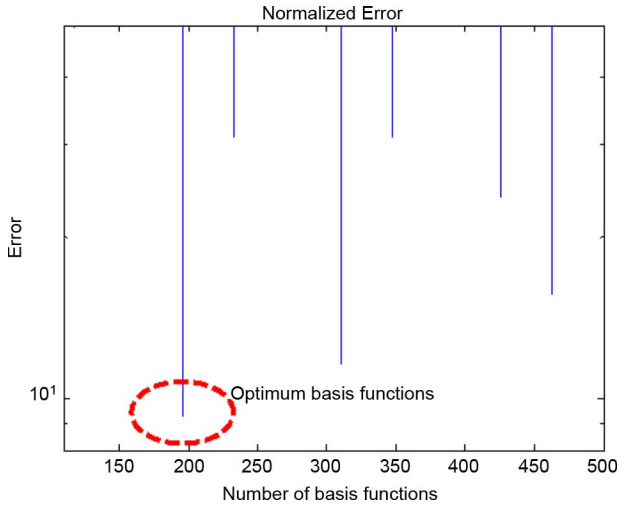

Fig. 17. Normalized error at $t = 0$ as a function of the number of basis coefficients using scheme B.

The energy profiles obtained using (30) and (31) are shown in Fig. 14. In the figure, q_{knee} resulting from scheme B is 110 while q_{knee} using scheme A is 40. The time-domain waveform from 40 basis coefficients using scheme A and from 110 basis coefficients using scheme B are shown in Fig. 15. There is a significant discrepancy between the FDTD result and SLeEC with scheme A toward the end of the time interval. This inaccuracy is due to the imprecise evaluation of the energy content which is dominated by $W_q[i]$ with large magnitude in early time, as per (33). However, the discrepancy that has been obtained using scheme A is not present in the waveform that has been obtained using scheme B in Fig. 15, which implies q_{knee} found by scheme B results in more accurate results.

C. Error Minimization at Time $t = 0$

Using energy analysis in the previous subsection, q_{knee} can be found which provides the minimal number of basis functions to describe the time-domain waveform. Now, the optimal number of basis function between q_{knee} and $q_{\max}$ should be chosen to ensure accuracy, which is the subject of this section.

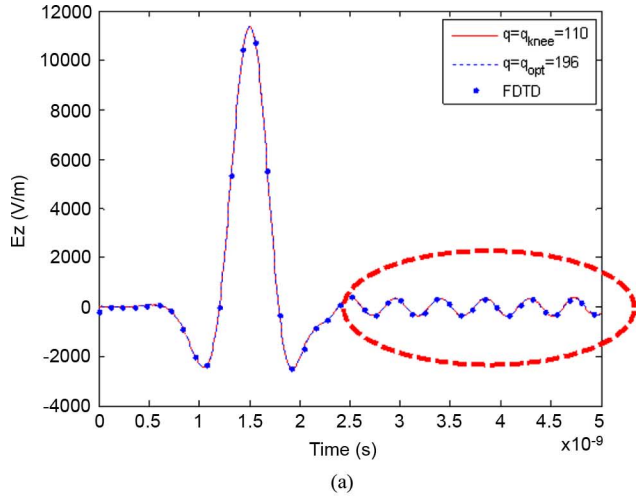

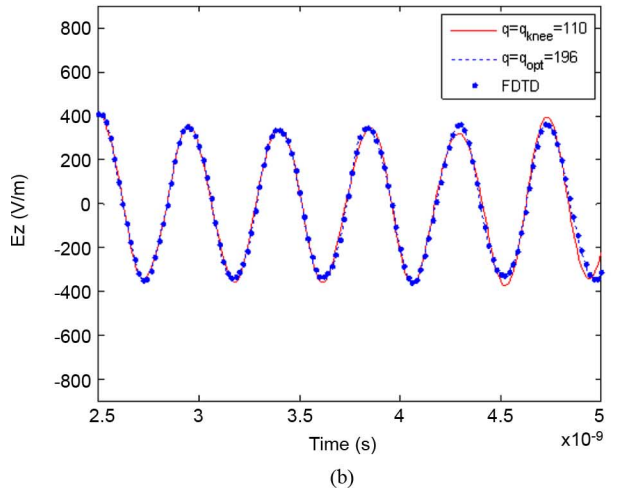

Fig. 18. Time-domain E_z field using q_{knee} and q_{opt} compared with FDTD: (a) 0–5 ns (b) Enlarged view of marked area in (a).

Let $E_{\text{exact}}(t)$ be the exact solution of the time-domain waveform which is represented as a sum of infinite number of weighted Laguerre basis functions where E_p represents pth Laguerre coefficient corresponding to the pth Laguerre basis function $\varphi_p(t)$

$$E_{\text{exact}}(t) = \sum_{p=0}^{\infty} E_p \cdot \varphi_p(t). \tag{34}$$

Using an approximation with N basis functions, the waveform is now represented as

$$E_{\text{approx}}(t) = \sum_{p=0}^{N-1} E_p \cdot \varphi_p(t). \tag{35}$$

The error $\epsilon(t)$ at time t can be written as

$$\epsilon(t) = E_{\text{exact}}(t) - E_{\text{approx}}(t) \tag{36}$$

$$= \sum_{p=0}^{\infty} E_p \cdot \varphi_p(t) - \sum_{p=0}^{N-1} E_p \cdot \varphi_p(t) \tag{37}$$

$$= \sum_{p=N}^{\infty} E_p \cdot \varphi_p(t) \tag{38}$$

Authorized licensed use limited to: Georgia Institute of Technology. Downloaded on November 19, 2009 at 13:11 from IEEE Xplore. Restrictions apply.

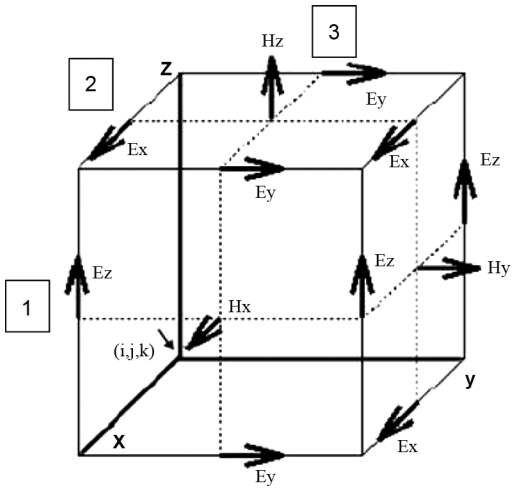

Fig. 19. Inefficient node numbering scheme (scheme 1).

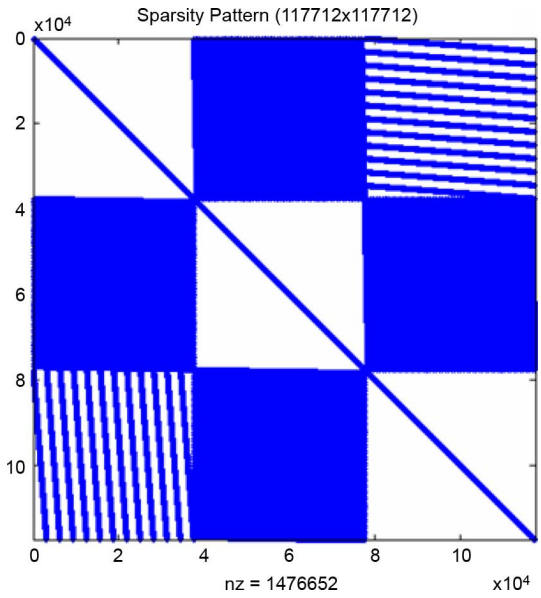

Fig. 20. Sparsity pattern of the A matrix from an inefficient node-numbering scheme (scheme 1).

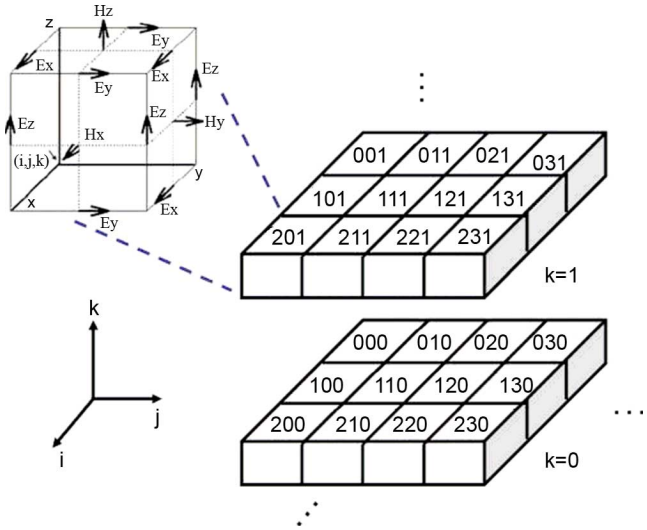

Fig. 21. Efficient node numbering scheme (scheme 2).

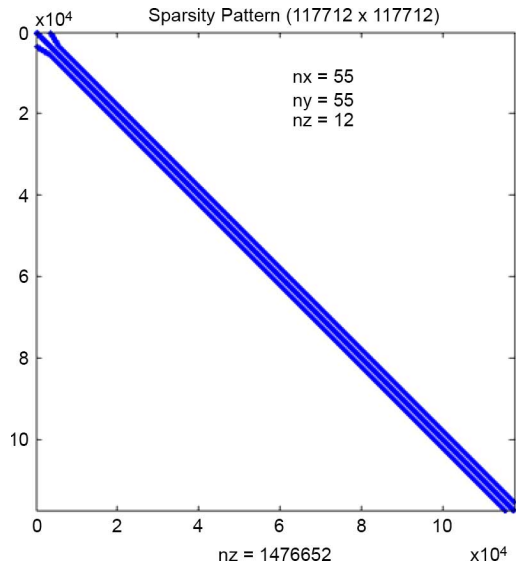

Fig. 22. Sparsity pattern of the A matrix suitable for LU decomposition (scheme 2).

$$= \lim_{M \to \infty} \sum_{p=N}^{N+M-1} E_p \cdot \varphi_p(t). \tag{39}$$

Since $E_{\text{exact}}(t)$ is approximated using the first N basis functions, E_N, E_{N+1}, E_{N+2}, ... are unknown while E_0, E_1, ..., E_{N-1} are known. Let us assume E_p where $p \geq N$ be a random variable with normal distribution (mean μ and variance σ^2) given by

$$E_p \sim N(0, \sigma^2) \text{ for } p \geq N. \tag{40}$$

Error at time $t = 0$ can be calculated as

$$\epsilon(0) = E_{\text{exact}}(0) - E_{\text{approx}}(0) \tag{41}$$

$$= \sum_{p=0}^{\infty} E_p \cdot \varphi_p(0) - \sum_{p=0}^{N-1} E_p \cdot \varphi_p(0) \tag{42}$$

$$= \sum_{p=N}^{\infty} E_p \cdot \varphi_p(0) \tag{43}$$

$$= \lim_{M \to \infty} M\mu. \tag{44}$$

The mean of E_p is

$$\mu = \lim_{M \to \infty} \frac{E_{\text{exact}}(0) - \sum_{q=0}^{N-1} E_p \cdot \varphi_p(0)}{M} = 0. \tag{45}$$

Thus, under the assumption that E_p for $p \geq N$ is a Gaussian random variable, its mean should be zero.

Since the sum of M Gaussian random variables with zero-mean and variance σ^2 is another Gaussian random variable with zero-mean and variance $M\sigma^2$, error at $t = 0$ is a Gaussian random variable with zero-mean and variance $M\sigma^2$ while M goes to infinity

$$\epsilon(0) \sim N\left(0, \lim_{M \to \infty} \sum_{p=1}^{M} \sigma^2\right). \tag{46}$$

Authorized licensed use limited to: Georgia Institute of Technology. Downloaded on November 19, 2009 at 13:11 from IEEE Xplore. Restrictions apply.

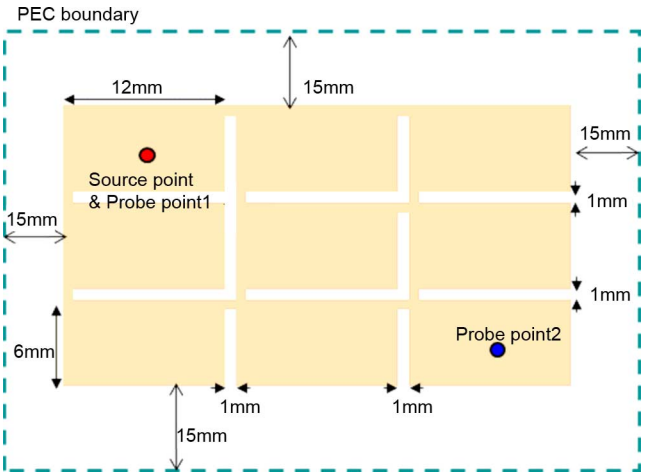

Fig. 23. Simulated EBG structure.

TABLE I
FDTD Versus SLeEC

Solver	♯ of Cells	Simulation Time	Memory	Speed-up
FDTD	15147	13 hours	4MB	3.7x
SLeEC	15147	3.5 hours	235MB	

Similarly, error at $t > 0$ also can be represented as a Gaussian random variable since it is the sum of weighted Gaussian random variables. While its mean is still zero, Since $\varphi_p(t) < 1$ for $t > 0$, as shown in Fig. 2, variance of error $\epsilon(t)$ is always smaller than variance of $\epsilon(0)$ for $t > 0$

$$Var(\epsilon(t)) = \lim_{M \longrightarrow \infty} \sum_{p=N}^{N+M-1} \varphi_p(t)^2 \sigma^2 \tag{47}$$

$$< \lim_{M \longrightarrow \infty} \sum_{p=N}^{N+M-1} \sigma^2 \tag{48}$$

$$< Var(\epsilon(0)). \tag{49}$$

Since $\varphi_p(t)$ is much smaller than 1 for most t, as shown in Fig. 2, $\mathrm{Var}(\epsilon(t))$ is much smaller than $\mathrm{Var}(\epsilon(0))$. Their probability density functions can therefore be approximated as shown in Fig. 16. The probability that $|\epsilon(0)|$ is greater than $|\epsilon(t)|$ for $t > 0$ is very small, which implies that $|\epsilon(0)| > |\epsilon(t)|$ for $t > 0$ in most cases. Therefore, in most cases, error at time $t > 0$ is bounded by error at time $t = 0$. Thus, minimizing error at time $t = 0$ is effective in reducing error at $t > 0$, which has been used as a measure to choose the optimal number of basis functions in this paper.

To illustrate error minimization, the example in Fig. 13 has been used again in this section. Normalized error at time $t = 0$ as a function of the number of basis coefficients is shown in Fig. 17. The number of basis functions that has minimum error at time $t = 0$ between q_{knee} and $q_{\max}$ is 196, as marked in the figure. Therefore, based on analysis, 196 is chosen as q_{opt}. Time-domain waveforms generated using q_{knee} and q_{opt} are shown in Fig. 18(a) and compared to FDTD. Both q_{knee} and q_{opt} seem to provide good correlation with FDTD. However,

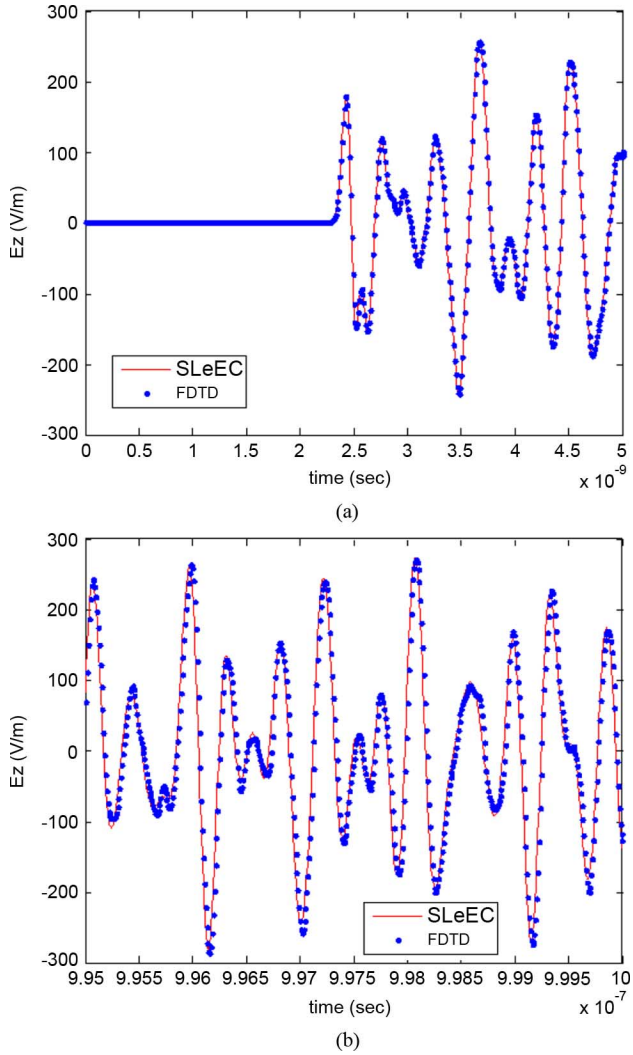

Fig. 24. Time-domain waveform at probe point 1 in the EBG structure: (a) From 0 to 5 ns; (b) from 995 ns to 1 μs.

a zoomed view shown in Fig. 18(b) reveals that q_{opt} provides better accuracy than q_{knee}.

VII. Node Numbering Scheme

SLeEC requires solving a matrix of the form $Ax = b$ at every iteration. However, LU decomposition has to be done only once because the A matrix stays constant throughout the iterations. For the Laguerre-domain companion model of the FDTD grid, two different node numbering schemes are considered. For both the schemes, the A matrix is sparse and structurally symmetric. The first scheme, which is labeled as scheme 1, is extremely inefficient for LU decomposition since it results in a nonbanded matrix while scheme 2 results in a sparse and banded matrix.

A Yee cell is shown in Fig. 19. The FDTD cells are cascaded in the *x*, *y*, and *z* dimensions to create a 3-D mesh. For simplicity, only a single cell is shown in Fig. 19, rather than an entire 3-D mesh. The cross sections of the FDTD cells that are parallel to the planes *xy*, *yz*, and the *zx* planes in the entire mesh are labeled 1, 2, and 3 in the figure. Let us assume that a domain consists of $nx \times ny \times nz$ cells. In scheme 1, all the nodes lying on Plane 1 for $k = 0, k = 1, \ldots k = nz - 1$ are labeled first; the nodes

Authorized licensed use limited to: Georgia Institute of Technology. Downloaded on November 19, 2009 at 13:11 from IEEE Xplore. Restrictions apply.

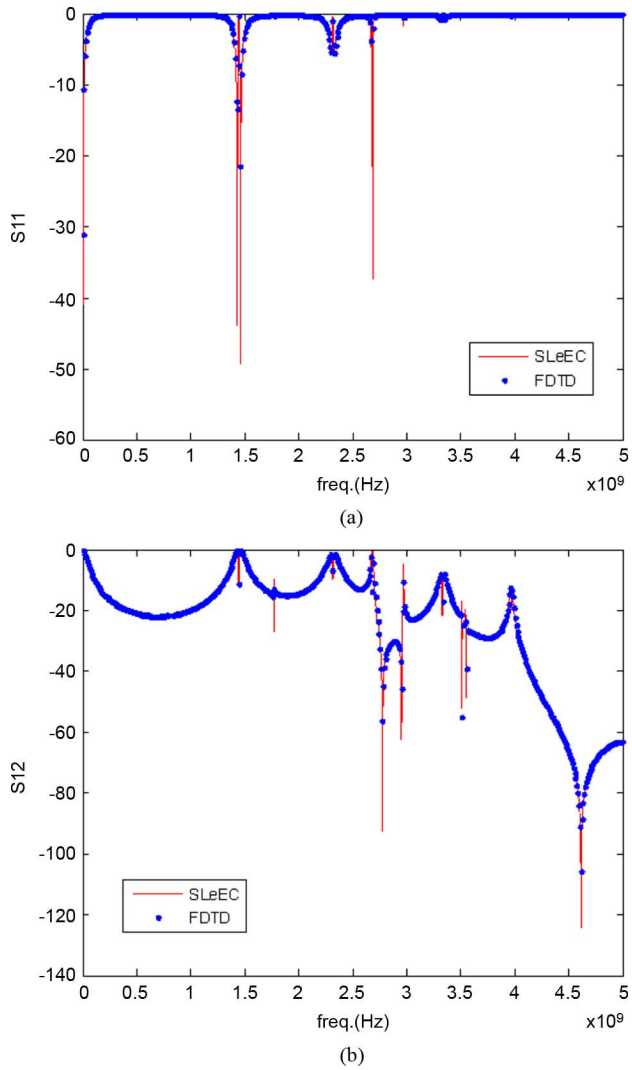

Fig. 25. *S*-parameters between probe points in the EBG structure: (a) S11; (b) S12.

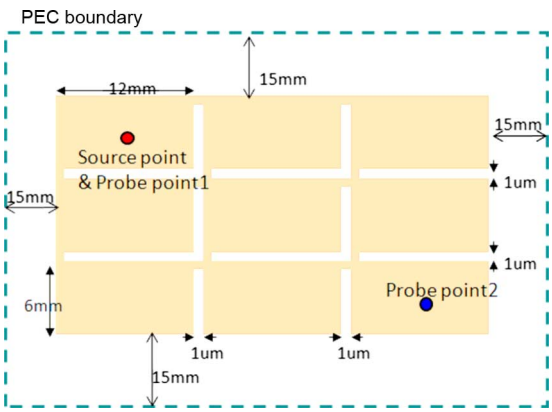

Fig. 26. Simulated EBG structure.

on Plane 2 for $i = 0, i = 1, \ldots, i = nx - 1$ are labeled next, followed by the nodes on Plane 3 for $j = 0, j = 1, \ldots j = ny - 1$. (nx, ny, nz) are the number of cells in the x, y, and z directions.

TABLE II
FDTD Versus SLeEC

Solver	♯ of Cells	Simulation Time	Memory	Speed-up
FDTD	15147	20 hours	4MB	67x
SLeEC	15147	18 minutes	220MB	

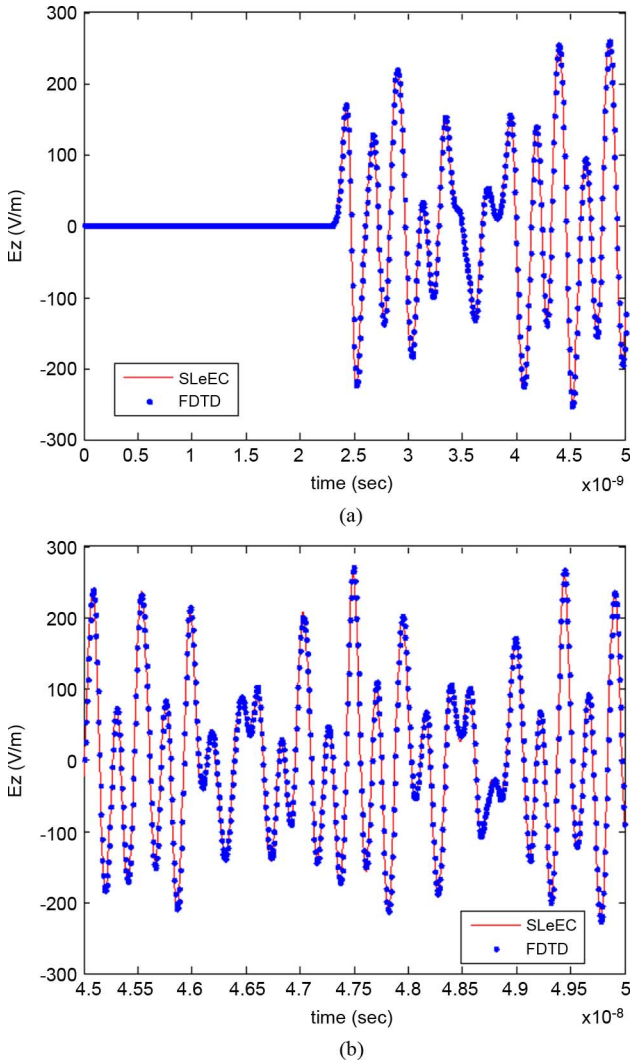

Fig. 27. Time-domain waveform at the probe point 1 in the EBG structure with narrow slit. (a) From 0 to 5 ns. (b) From 45 to 50 ns.

The sparsity pattern of the A matrix that is of dimension $117\,712 \times 117\,712$ ($117\,712$ unknowns) resulting from scheme 1 is shown in Fig. 20. The number of nonzero entries in matrix A is $1\,476\,652$. The structural symmetry can be clearly seen from the pattern. The matrix is always structurally symmetric for the PEC and the PMC boundary conditions, regardless of the structure that is being modeled.

The sparsity pattern of the A matrix from scheme 1 is not desirable due to its bandwidth which contains a large number of nonzero entries in L and U matrix after LU decomposition. Thus, node ordering scheme that makes A matrix banded is preferable.

Here, an alternate method (scheme 2) is proposed for the A matrix to become banded. In scheme 2, the nodes are numbered on a cell by cell basis.

Authorized licensed use limited to: Georgia Institute of Technology. Downloaded on November 19, 2009 at 13:11 from IEEE Xplore. Restrictions apply.

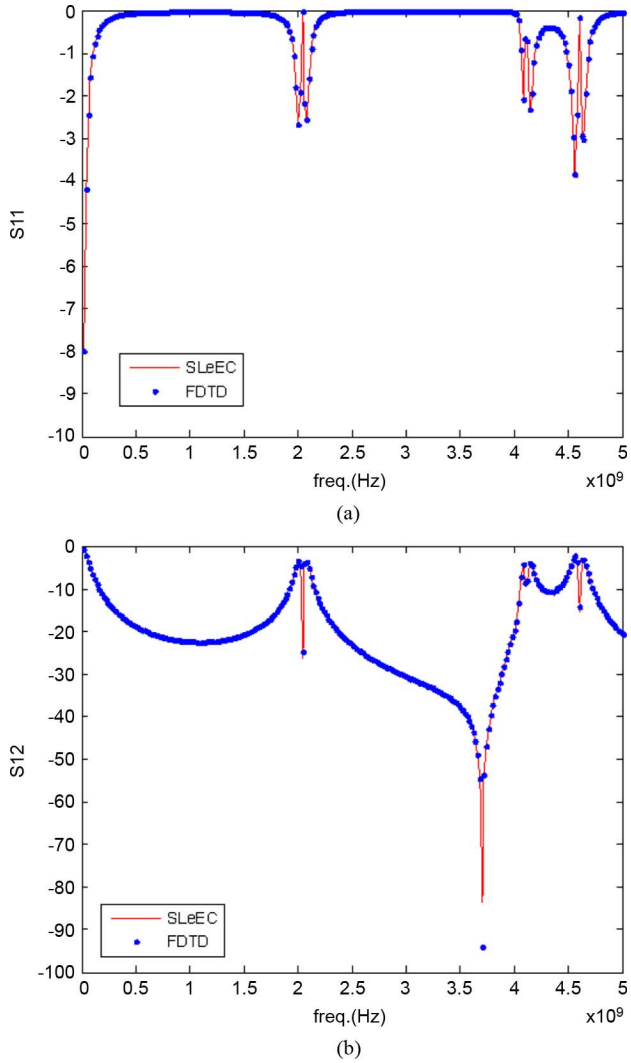

Fig. 28. *S*-parameters between probe points in the EBG structure with narrow slit: (a) S11; (b) S12.

Let us assume that a domain consists of $nx \times ny \times nz$ cells and label an ith Yee cell on jth row on kth plane as cell (ijk), as shown in Fig. 21.

The nodes within a cell(000) at the corner are numbered first, and the nodes within an adjacent cell in x direction, cell(100), are labeled next. In case of the shared nodes between cell(000) and cell(100), since all nodes within cell(000) are numbered prior to the numbering of the nodes within cell(100), the shared nodes are skipped in the numbering of the nodes within cell(100). Next, the nodes within a cell(200) are numbered in a similar fashion, and the numbering continues until it reaches cell$(nx00)$. As a similar numbering process is applied to the nodes within cells at other rows and planes, all nodes in the domain are numbered.

Due to the local behavior of Maxwell equations on a Yee cell, this form of node numbering can lead to the A matrix being banded.

The sparsity pattern resulting from scheme 2 for the same structure is shown in Fig. 22. The A matrix is banded, and therefore the number of nonzero entries in L and U factors are much less than the matrix resulting from scheme 1.

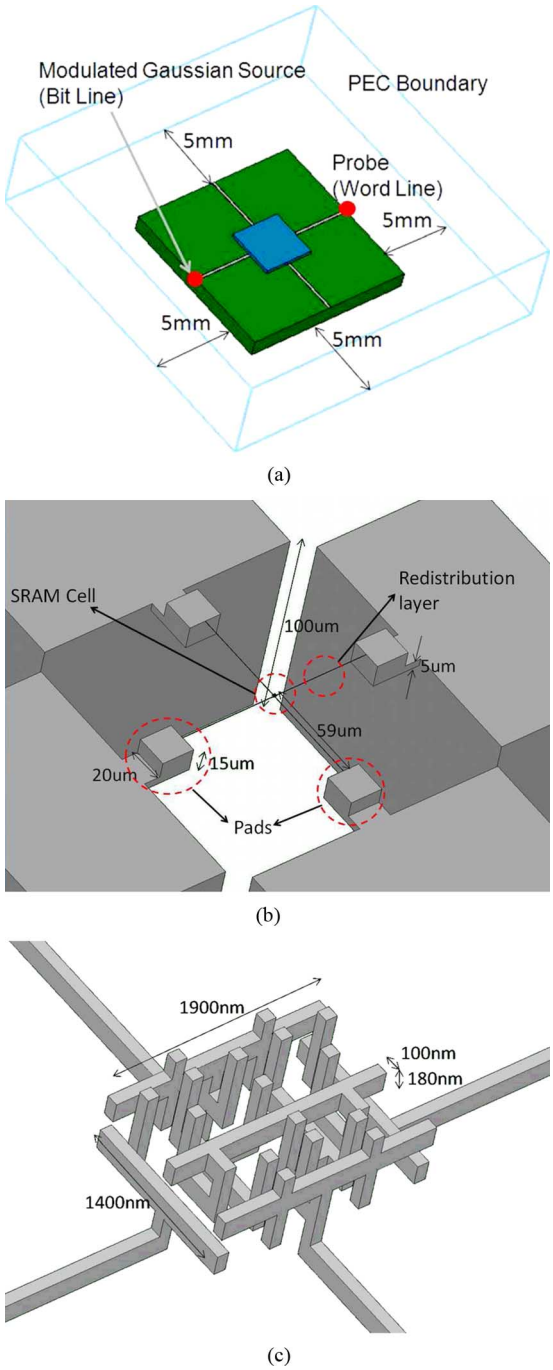

Fig. 29. Chip-package structure with multiscale features. (a) Package structure. (b) Redistribution layer and package bump. (c) Chip structure.

VIII. Multiscale Test Cases

A. Test Case 1: EBG Structure

As an example, consider the EBG structure shown in Fig. 23. The EBG patch dimension is 6 mm $\times$ 12 mm and dimension of bridge between EBG patches is 1 mm $\times$ 1 mm with a dielectric thickness of 200 μm and conductor thickness of 30 μm. The EBG structure is referenced to a continuous ground plane beneath it. The structure is surrounded by PEC boundary with a gap of 15 mm. The current source is excited between two conductors at the point shown in Fig. 23 and the vertical component

Authorized licensed use limited to: Georgia Institute of Technology. Downloaded on November 19, 2009 at 13:11 from IEEE Xplore. Restrictions apply.

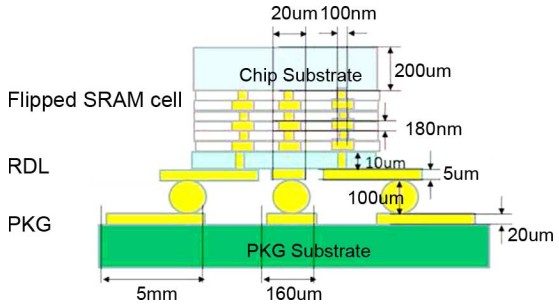

Fig. 30. Cross section of the different metal layers.

of the electric field is probed at the probe points shown in the figure. The source waveform is a Gaussian derivative. The simulation has been done up to 1 μs using the proposed method in Section V. The simulations were run on a Pentium quad core, 2.4 GHz processor with 4 GB RAM. The comparison of simulation time between SLeEC and FDTD is shown in Table I.

In Fig. 24, the simulated time-domain waveform using SLeEC at probe point 1 is shown and compared with the FDTD method. They show excellent correlation until 1 μs though SLeEC took 3.7x lesser time to simulate the structure. The *s*-parameters between the two probe points are also extracted from the simulated time-domain waveforms, as shown in Fig. 25. SLeEC and FDTD show very good correlation in the frequency domain as well.

B. Test Case 2: EBG Structure With Narrow Slit

This structure is similar to the previous EBG structure as shown in Fig. 26. However, the dimension of bridge between EBG cells is reduced to $1\ \mu\mathrm{m} \times 1\ \mu\mathrm{m}$. Since the dimension of the mesh is very small at the $1\ \mu\mathrm{m} \times 1\ \mu\mathrm{m}$ bridge, the FDTD method requires a very small time step of $4fs$ and hence takes long time to simulate, as shown in Table II

The simulated time-domain waveform using SLeEC at probe point 1 are shown in Fig. 27 and compared with the FDTD method. They show very good correlation until 50 ns. A 67x speedup was possible using SLeEC as compared to the FDTD method for this example. The *S*-parameters extracted from the simulated time-domain waveform are also shown in Fig. 28, which show good correlation with the FDTD method.

C. Test Case 3: Chip-Package Structure

Results from chip-package co-simulation is presented in this subsection. The package structure is shown in Fig. 29(a). A chip that contains SRAM cell is flipped and attached on a package with redistribution layer. The on-chip structures, along with the interface between the chip and the package, are shown in Fig. 29(b). The zoom of the center region in Fig. 29(b) is shown in Fig. 29(c). The on-chip structures in Fig. 29(c) represent the interconnects in M1 and M2 layers of an SRAM cell. The structures that have been modeled are the on-chip interconnects in metal layers M1 and M2, connected by vias and routed on the redistribution layer, through the solder pads, to the package and routed as package-level interconnects.

An important feature of the chip-package structure is its multiscale dimensions, as shown in Fig. 30. The on-chip structure is

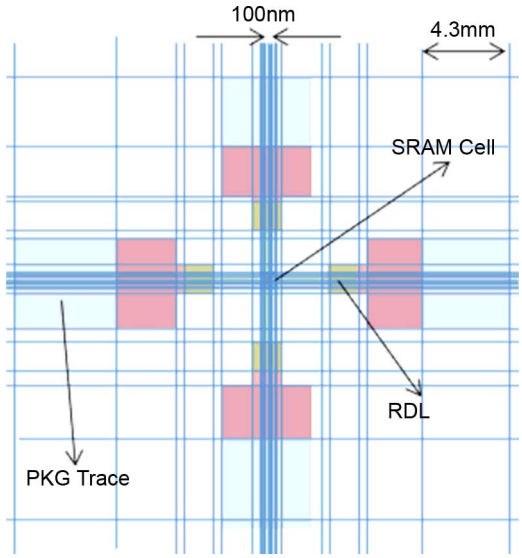

Fig. 31. Nonuniform mesh simulated using SLeEC.

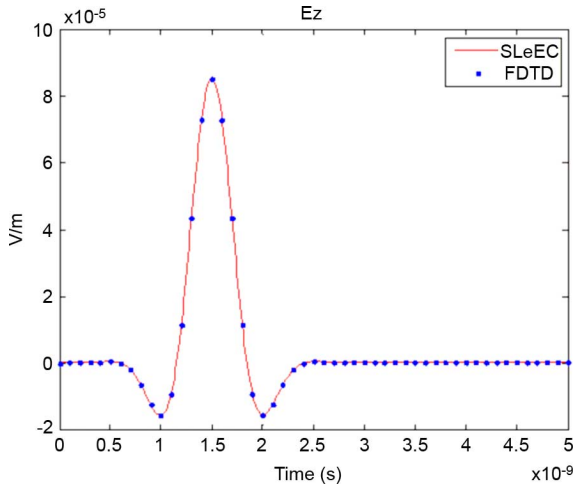

Fig. 32. SLeEC and FDTD results of the chip-package structure.

in the nanometer scale, the dimensions of the structure present at the interface between the chip and the package, such as the redistribution layer, solder pads, are in the micrometer scale, and package structures such as the power-ground planes are in the millimeter range. The on-chip structures that are in the nanometer scale require a very fine mesh, and therefore the simulation time can become prohibitively large using the FDTD method due to the Courant condition.

A nonuniform mesh has been used here, as shown in Fig. 31. Meshes shown in the figure are not proportional to actual mesh dimensions. Meshes at the center are very fine due to the SRAM chip structure in the center. The scale difference in this example is 1:50 000.

A modulated Gaussian source current was excited at the location marked *source* in Fig. 29(a) and the time-domain response of the electric field at the location marked *probe* in Fig. 29(a) is shown in Fig. 32. There is excellent correlation between SLeEC and FDTD. The field snapshots at 1, 1.25, and 1.5 ns are shown in Fig. 33. The propagation of the electromagnetic wave through the structure can be seen in Fig. 33

Authorized licensed use limited to: Georgia Institute of Technology. Downloaded on November 19, 2009 at 13:11 from IEEE Xplore. Restrictions apply.

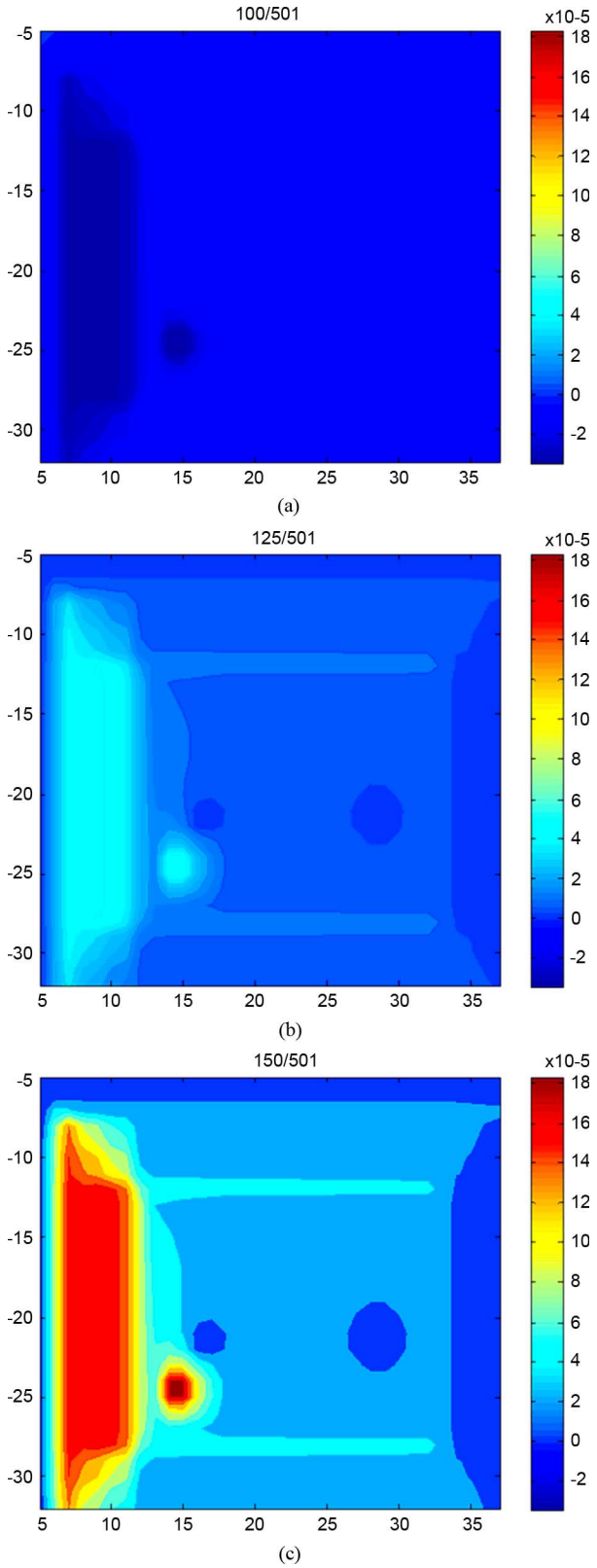

Fig. 33. E_z field snapshots at (a) 1 ns, (b) 1.25 ns, (c) 1.5 ns.

The number of cells used in the simulation was 26,144. FDTD took over one day to run, while SLeEC takes only 9 min to complete, as shown in Table III. The simulation was run on the Pentium quad core, 2.4 GHz processor with 4 GB RAM.

TABLE III
FDTD Versus SLeEC

Solver	♯ of Cells	Simulation Time	Memory	Speed-up
FDTD	26144	30 hours	4.8MB	200x
SLeEC	26144	9 minutes	480MB	

IX. Conclusion

In this paper, the Laguerre-FDTD method has been used for simulation of multiscale structures. The Laguerre-FDTD has been applied by converting it into a circuit representation (SLeEC). Two major issues have been addressed in this paper, namely, simulatiing over long time and choosing the optimal number of basis functions. The accuracy and advantage of this method have been validated by comparing it with FDTD on several examples arising in packaging.

Acknowledgment

The authors would like to thank Dr. E. Engin, San Diego State University, San Diego, CA, for helpful discussions during the early part of the formulation.

References

[1] Y. Chung, T. K. Sarkar, B. H. Jung, and M. Salazar-Palma, "An unconditionally stable scheme for the finite-difference time-domain method," *IEEE Trans. Microwave Theory Tech.*, vol. 51, no. 3, pp. 697–704, Mar. 2003.

[2] Z. Ji, T. K. Sarkar, B. H. Jung, Y. Chung, M. Salazar-Palma, and M. Yuan, "A stable solution of time domain electric field integral equation for thin-wire antennas using the Laguerre polynomials," *IEEE Trans. Antennas Propag.*, vol. 52, no. 10, pp. 2641–2649, Oct. 2004.

[3] M. Yuan, T. K. Sarkar, B. Jung, Z. Ji, and M. Salazar-Palma, "A comparison of performance of three orthogonal polynomials in extraction of wide-band response using early time and low frequency data," *IEEE Trans. Antennas Propag.*, vol. 52, no. 7, pp. 1740–1750, Jul. 2004.

[4] S. G. Garcia, T. Lee, and S. C. Hagness, "On the accuracy of the ADI-FDTD method," *IEEE Antennas Wireless Propag. Lett.*, vol. 1, pp. 31–34, 2002.

[5] M. Krumpholz and L. Katehi, "MRTD: New time-domain schemes based on multiresolution analysis," *IEEE Trans. Microwave Theory Tech.*, vol. 44, no. 4, pp. 555–571, Apr. 1996.

[6] R. Holland and L. Simpson, "Finite-difference analysis of EMP coupling to thin struts and wires," *IEEE Trans. Electromagn. Compatibil.*, vol. EMC-23, no. 2, pp. 88–97, May 1981.

[7] K. Srinivasan, M. Swaminathan, and E. Engin, "Overcoming limitations of Laguerre-FDTD for fast time-domain EM simulation," in *IEEE MTT-S Int. Microwave Symp.*, Jun. 2007, pp. 891–894.

[8] K. Srinivasan, E. Engin, and M. Swaminathan, "Fast FDTD simulation using Laguerre polynomials in MNA framework," presented at the Int. Symp. Electromagn. Compatibil., Honolulu, HI, Jul. 2007.

[9] K. Srinivasan, M. Swaminathan, and E. Engin, "Enhancement of Laguerre-FDTD with initial conditions for fast transient EM/Circuit simulation," presented at the Electronic Compon. Technol. Conf., Reno, NV, May 2007.

[10] K. Srinivasan, E. Engin, and M. Swaminathan, "Fast FDTD simulation of multiscale 3-D models using Laguerre-MNA," in *IEEE Workshop Signal Propag. Interconnects*, May 2007, pp. 141–144.

[11] K. Srinivasan, P. Yadav, E. Engin, and M. Swaminathan, "Choosing the right number of basis functions in multiscale transient simulation using Laguerre polynomials," in *Electr. Performance Electron. Packag.*, Oct. 2007, pp. 291–294.

[12] M. Ha, K. Srinivasan, and M. Swaminathan, "Chip-package co-simulation with multiscale structures," in *Electr. Performance Electron. Packag.*, Oct. 2008, pp. 339–342.

[13] S. M. Rao, *Time-domain Electromagnetics*. New York: Academic, 2006.

[14] L. T. Pillage, R. A. Rohrer, and C. Visweswariah, *Electronic Circuit and System Simulation Methods*. New York: McGraw-Hill, 1994.

Authorized licensed use limited to: Georgia Institute of Technology. Downloaded on November 19, 2009 at 13:11 from IEEE Xplore. Restrictions apply.

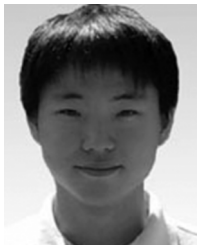

Myunghyun Ha received the B.S. and M.S. degrees in electrical engineering from the Korea Advanced Institute of Science and Technology (KAIST), Daejeon, South Korea, in 2004 and 2007, respectively. He is currently pursuing the Ph.D. degree in electrical and computer engineering at Georgia Institute of Technology, Atlanta.

His research interest is time and frequency domain electromagnetic field simulation method using orthogonal functions that enables chip-package co-simulation.

Krishna Srinivasan received the B.A.Sc. degree in computer engineering from the University of Toronto, Toronto, ON, Canada, and the M.S. and Ph.D. degrees in electrical engineering from the Georgia Institute of Technology, Atlanta, in 2008.

He did his summer internship at IBM, Essex Junction, VT. He is now working at Intel, Chandler, AZ. His research interests are in computational electromagnetics and digital/RF systems.

Madhavan Swaminathan received the B.E. degree in electronics and communication from the University of Madras, Chennai, India, and the M.S. and Ph.D. degrees in electrical engineering from Syracuse University, Syracuse, NY.

He is currently the Joseph M. Pettit Professor in Electronics in the School of Electrical and Computer Engineering, Georgia Tech, the Associate Director of the SRC Interconnect and Packaging Center and directs the design activities at the Packaging Research Center. He was the Deputy Director of the Packaging Research Center, Georgia Tech from 2004 to 2008. He is the co-founder of Jacket Micro Devices, a company specializing in integrated devices and modules for wireless applications and the founder of E-System Design, an EDA company focusing on CAD development for integrated microsystems. Prior to joining Georgia Tech, he was with the Advanced Packaging Laboratory at IBM working on packaging for super computers. He has over 300 publications in refereed journals and conferences, has co-authored three book chapters, has 17 issued patents, and has several patents pending. He is also the principal author of the book "Power Integrity Modeling and Design for Semiconductors and Systems, Prentice Hall, 2007" and co-editor of the book "Introduction to System on Package (SOP), McGraw Hill, 2008". While at IBM, he reached the second invention plateau. His research interests are in mixed signal micro-system and nano-system integration with emphasis on design, CAD, electrical test and new architectures.

Dr. Swaminathan has been a guest editor for the IEEE TRANSACTIONS ON ADVANCED PACKAGING and IEEE TRANSACTIONS ON MICROWAVE THEORY AND TECHNIQUES. He was the Associate Editor of the IEEE TRANSACTIONS ON COMPONENTS AND PACKAGING TECHNOLOGY. He is the recipient of the 2002 Outstanding Graduate Research Advisor Award from the School of Electrical and Computer Engineering, Georgia Tech and the 2003 Outstanding Faculty Leadership Award for the mentoring of graduate research assistants from Georgia Tech. He is also the recipient of the 2003 Presidential Special Recognition Award from IEEE CPMT Society for his leadership of TC-12 and the IBM Faculty Award in 2004 and 2005. He has also served as the co-author and advisor of a number of outstanding student paper awards at EPEP'00, EPEP'02, EPEP'03, EPEP'04, EPEP'08, ECTC'98, ECTC'08, APMC'05, and the 1997 IMAPS Education Award. He is the recipient of the Shri. Mukhopadyay best paper award at the International Conference on Electromagnetic Interference and Compatibility (INCEMIC), Chennai, India, 2003, the 2004 best paper award in the IEEE Transactions on Advanced Packaging, the 2004 commendable paper award in the IEEE Transactions on Advanced Packaging and the best poster paper award at ECTC'04 and '06. In 2007, Dr. Swaminathan was recognized for his research through the Technical Excellence Award given by Semiconductor Research Corporation (SRC) and Global Research Corporation (GRC). He served as the Co-Chair for the 1998 and 1999 IEEE Topical Meeting on Electrical Performance of Electronic Packaging (EPEP), served as the Technical and General Chair for the IMAPS Next Generation IC & Package Design Workshop, serves as the Chair of TC-12, the Technical Committee on Electrical Design, Modeling and Simulation within the IEEE CPMT society and was the Co-Chair for the 2001 IEEE Future Directions in IC and Package Design Workshop. He is the co-founder of the IMAPS Next Generation IC & Package Design Workshop and the IEEE Future Directions in IC and Package Design Workshop. He also serves on the technical Program committees of EPEP, Signal Propagation on Interconnects workshop, Solid State Devices and Materials Conference (SSDM), Electronic Components and Technology Conference (ECTC), and International Symposium on Quality Electronic Design (ISQED). He is the founder of Electrical Design of Advanced Packaging and Systems, a Signal Integrity Symposium in the Asian region.

Authorized licensed use limited to: Georgia Institute of Technology. Downloaded on November 19, 2009 at 13:11 from IEEE Xplore. Restrictions apply.